On the consistency of three-dimensional magnetohydrodynamical lattice Boltzmann models

J. Li, K.T.E. Chua, H.Y. Li, V.-T. Nguyen, D.J. Wise, G.X. Xu, C.W. Kang, and W.H.R. Chan*

Institute of High Performance Computing (IHPC), Agency for Science, Technology and Research (A*STAR), 1 Fusionopolis Way, #16-16, Connexis North, Singapore 138632, Republic of Singapore

Abstract

The lattice Boltzmann method (LBM) for magnetohydrodynamics (MHD) was first developed for two-dimensional (2D) flows. The magnetic component of the Lorentz force is obtained from the divergence of the Maxwell stress tensor, which is recovered by an appropriate modification to the LBM equilibrium distribution function for the solution of the velocity field. Although this method has subsequently been applied to three-dimensional (3D) flows, we show that several common modifications of the 3D equilibrium distribution function cannot simultaneously recover the Maxwell stress tensor and conserve mass exactly. Our study brings attention to this theoretical issue since such inconsistent models have been used in recent 3D LBM MHD simulations. Both requirements can be simultaneously satisfied by incorporating an additional model term to the 3D equilibrium distribution function. Three variants of Hunt's flow in a rectangular channel are considered to illustrate the undesirable consequences of using inconsistent models: 1) flow driven by a pressure difference, 2) flow driven by an external body force, and 3) inclusion of a streamwise gradient in magnetic pressure. While spurious errors were observed using inconsistent models due to the violation of mass conservation or inaccuracy in the Maxwell stress tensor, the consistent model always achieves the correct solutions in these cases and is recommended for 3D MHD simulations.

1. Introduction

The lattice Boltzmann method (LBM) [1, 2, 3] is an efficient and scalable numerical method for the computation of fluid flows and is well suited for complex boundary conditions that can be challenging for finite-element and finite-volume methods. It has been employed in a variety of multi-physics situations, including microfluidics [4], porous-media flows [5, 6, 7, 8], phase-change heat transfer [8, 9, 10], as well as magnetohydrodynamical (MHD) flows [11], including those relevant to fusion energy systems [12]. In MHD flows, the motion of an electrically conductive fluid induces electric currents and magnetic fields, such as in the presence of an external magnetic field. The flow velocity can be significantly modified by the generated Lorentz force, particularly from motion perpendicular to the magnetic field lines. MHD flows in practical geometries and set-ups, such as open channels [13, 14] with field gradients [15] and free surfaces [16, 17], are increasingly important for the design, optimisation, and future operation of fusion reactors and energy systems, which are necessary in the global push towards sustainability.

In the widely used LBM scheme for the magnetic induction formulation by Dellar [18], the magnetic component of the Lorentz force is absorbed into the stress tensor

*Ronald_Chan@ihpc.a-star.edu.sg

conventionally placed on the left-hand side of the momentum equation, namely as $-\vec{J} \times \vec{B} = -(\mu^{-1}\nabla \times \vec{B}) \times \vec{B}$, and converted into $\mu^{-1}\nabla \cdot \left(\frac{1}{2}B^2\mathbf{I} - \vec{B}\otimes\vec{B}\right)$, where $\vec{J}$ is the electric current, $\vec{B}$ is the magnetic field with magnitude B, μ is the magnetic permeability of the fluid, $\mathbf{I}$ is the identity tensor, $\otimes$ is the dyadic product operator, and $\left(\frac{1}{2}B^2\mathbf{I} - \vec{B}\otimes\vec{B}\right)$ is the Maxwell stress tensor. Correspondingly, the equilibrium distribution function f_α^{eq} of the LBM flow solver is changed to $f_\alpha^{\mathrm{MHD(eq)}}$ as follows

$$f_\alpha^{\mathrm{MHD(eq)}} = f_\alpha^{\mathrm{eq}} + \frac{\omega_\alpha}{2c_s^4\mu}\left[C_B(\vec{B}\cdot\vec{B})(\vec{e}_\alpha\cdot\vec{e}_\alpha) - (\vec{e}_\alpha\cdot\vec{B})^2\right], \tag{1}$$

where $\vec{e}_\alpha$ and ω_α are, respectively, the lattice velocity and weight factor in the $\alpha \in [0, Q-1]$ direction of the flow solver, Q is the number of lattice velocities, $c_s = \Delta x/(\sqrt{3}\Delta t)$ is the sound speed used in LBM, Δx and Δt are, respectively, the lattice distance and time step, and C_B is the model constant that will be discussed in the current study. The magnetic field $\vec{B}$ is obtained using a separate vector-valued LBM routine [18] to solve the magnetic induction equation

$$\frac{\partial\vec{B}}{\partial t} = \nabla \times (\vec{u} \times \vec{B}) + \frac{1}{\mu\sigma}\Delta\vec{B}, \tag{2}$$

where $\vec{u}$ is the flow velocity, σ is the electrical conductivity, and $\eta = 1/(\mu\sigma)$ is the magnetic diffusivity. The critical constraint $\nabla \cdot \vec{B} = 0$ is automatically enforced in LBM with high accuracy, which is a remarkable advantage over traditional computational fluid dynamical algorithms that usually require a divergence cleaning process. The detailed algorithm used to couple the flow and magnetic solvers is provided in the Appendix.

For physical consistency, the second moment of $f_\alpha^{\mathrm{MHD(eq)}}$, expressed in terms of $\vec{e}_\alpha$, should recover the Maxwell stress tensor as follows

$$\sum_{\alpha=0}^{Q-1}\vec{e}_\alpha\otimes\vec{e}_\alpha f_\alpha^{\mathrm{MHD(eq)}} = \sum_{\alpha=0}^{Q-1}\vec{e}_\alpha\otimes\vec{e}_\alpha f_\alpha^{\mathrm{eq}} + \mu^{-1}\left(\frac{1}{2}B^2\mathbf{I} - \vec{B}\otimes\vec{B}\right), \tag{3}$$

where $\sum_{\alpha=0}^{Q-1}\vec{e}_\alpha\otimes\vec{e}_\alpha f_\alpha^{\mathrm{eq}} = \rho\vec{u}\otimes\vec{u} + p\mathbf{I}$ is required to recover the original compressible Navier–Stokes equations. Here, ρ is the density and $p = c_s^2\rho$ is the thermodynamic pressure. Variables and constants with physical (SI) units are used in our formulation, which can be achieved by having Δx and $c \equiv \Delta x/\Delta t$ take arbitrary values different from unity. Since the magnetic component of the Lorentz force, $\vec{J} \times \vec{B}$, is included through the modified equilibrium distribution function $f_\alpha^{\mathrm{MHD(eq)}}$, an LBM force model is unnecessary and $\vec{u}$ is computed without an explicit force term in the absence of other force sources.

For 3D LBM MHD models, different values for the model constant C_B have been used in past simulations, e.g., $C_B = 1/2$ [19, 20], $C_B = 1/3$ [21, 22, 23], and $C_B = 1$ [24]. As we show in the remainder of this paper, arbitrary modifications of C_B can lead to inconsistencies in recovering the correct Maxwell stress tensor and in mass conservation. For ease of reference, variants of the 3D version of Eq. (1) with different C_B values are henceforth referred to as the so-called "inconsistent models". The paper is structured as follows: Section 2 describes the recovery of the Maxwell stress tensor from the equilibrium distribution function, while Section 3 discusses the requirements on C_B to maintain mass conservation. We introduce a consistent model that simultaneously recovers the Maxwell stress tensor and conserves mass in Section 4. In Section 5, we present simulation results comparing the consistent model with inconsistent models in various rectangular channel flows. Finally, our conclusions are provided in Section 6.

2. Recovering the Maxwell stress tensor

The model constant C_B in Eq. (1) was set to $1/2$ for the D2Q9 lattice model in the seminal work by Dellar [18]. This modification for incorporating the Lorentz force has more recently been extended to the D3Q27 lattice model with C_B set to $1/2$ and 1 in Refs. [19] and [24], respectively, and the D3Q19 lattice model with $C_B = 1/2$ [20]. The obtained $f_\alpha^{\mathrm{MHD(eq)}}$ is then used to compute the equilibrium moments for the corresponding multi-relaxation-time simulations.

We verify the value of the constant C_B that recovers the Maxwell stress tensor for various lattice models. For the D2Q9 model, we have $c_s = c/\sqrt{3}$, $\omega_0 = 4/9$, $\omega_{\alpha\in[1,4]} = 1/9$, $\omega_{\alpha\in[5,8]} = 1/36$, and

$$\begin{cases} |e_{\alpha 1}\rangle = c[0,1,0,-1,0,1,-1,-1,1]^{\mathrm{T}}, \\ |e_{\alpha 2}\rangle = c[0,0,1,0,-1,1,1,-1,-1]^{\mathrm{T}}. \end{cases} \tag{4}$$

Using the following identity

$$\sum_{\alpha=0}^{Q-1} \omega_\alpha e_{\alpha i} e_{\alpha j} e_{\alpha k} e_{\alpha l} = \frac{c^4}{9}\left(\delta_{ij}\delta_{kl} + \delta_{ik}\delta_{jl} + \delta_{il}\delta_{jk}\right), \tag{5}$$

we obtain the corresponding second moment

$$\begin{aligned} \sum_{\alpha=0}^{Q-1} \vec{e}_\alpha \otimes \vec{e}_\alpha \left(f_\alpha^{\mathrm{MHD(eq)}} - f_\alpha^{\mathrm{eq}}\right) &= \sum_{\alpha=0}^{Q-1} \vec{e}_\alpha \otimes \vec{e}_\alpha \frac{\omega_\alpha}{2c_s^4\mu}\left[C_B(\vec{B}\cdot\vec{B})(\vec{e}_\alpha\cdot\vec{e}_\alpha) - \left(\vec{e}_\alpha\cdot\vec{B}\right)^2\right] \\ &= \frac{9C_B}{2c^4\,\mu} c^4 \left(0 + \frac{1\times 2\times 1}{9} + \frac{1\times 4\times 2}{36}\right)(\vec{B}\cdot\vec{B})\mathbf{I} - \frac{1}{2\mu}\left[(\vec{B}\cdot\vec{B})\mathbf{I} + 2\vec{B}\otimes\vec{B}\right] \\ &= \frac{4C_B}{2\mu}(\vec{B}\cdot\vec{B})\mathbf{I} - \frac{1}{2\mu}\left[(\vec{B}\cdot\vec{B})\mathbf{I} + 2\vec{B}\otimes\vec{B}\right] = \frac{4C_B - 1}{2\mu}(\vec{B}\cdot\vec{B})\mathbf{I} - \frac{1}{\mu}\vec{B}\otimes\vec{B}. \end{aligned} \tag{6}$$

The Maxwell stress tensor is recovered only if $C_B = 1/2$, as used in Ref. [18].

For the D3Q27 model, we have $c_s = c/\sqrt{3}$, $\omega_{\mathrm{centre}} = 8/27$ for $\alpha = 0$, $\omega_{\mathrm{face}} = 2/27$ for $\alpha \in [1,6]$, $\omega_{\mathrm{edge}} = 1/54$ for $\alpha \in [7,18]$, $\omega_{\mathrm{corner}} = 1/216$ for $\alpha \in [19,26]$, and

$$\begin{cases} |e_{\alpha 1}\rangle = c[0,1,-1,0,0,0,0,1,-1,1,-1,1,-1,1,-1,0,0,0,0,1,-1,1,-1,1,-1,1,-1]^{\mathrm{T}}, \\ |e_{\alpha 2}\rangle = c[0,0,0,1,-1,0,0,1,1,-1,-1,0,0,0,0,1,-1,1,-1,1,1,-1,-1,1,1,-1,-1]^{\mathrm{T}}, \\ |e_{\alpha 3}\rangle = c[0,0,0,0,0,1,-1,0,0,0,0,1,1,-1,-1,1,1,-1,-1,1,1,1,1,-1,-1,-1,-1]^{\mathrm{T}}. \end{cases} \tag{7}$$

The corresponding second moment is

$$\sum_{\alpha=0}^{Q-1} \vec{e}_\alpha \otimes \vec{e}_\alpha \left(f_\alpha^{\mathrm{MHD(eq)}} - f_\alpha^{\mathrm{eq}}\right) = \frac{5C_B - 1}{2\mu}(\vec{B}\cdot\vec{B})\mathbf{I} - \frac{1}{\mu}\vec{B}\otimes\vec{B}, \tag{8}$$

which recovers the Maxwell stress tensor only if $C_B = 2/5$ (not $C_B = 1/2$ [19] or $C_B = 1$ [24]).

For the widely used D3Q19 model, we have $c_s = c/\sqrt{3}$, $\omega_{\mathrm{centre}} = 1/3$ for $\alpha = 0$, $\omega_{\mathrm{face}} = 1/18$ for $\alpha \in [1,6]$, $\omega_{\mathrm{edge}} = 1/36$ for $\alpha \in [7,18]$, and

$$\begin{cases} |e_{\alpha 1}\rangle = c[0,1,-1,0,0,0,0,1,-1,1,-1,1,-1,1,-1,0,0,0,0]^{\mathrm{T}}, \\ |e_{\alpha 2}\rangle = c[0,0,0,1,-1,0,0,1,1,-1,-1,0,0,0,0,1,-1,1,-1]^{\mathrm{T}}, \\ |e_{\alpha 3}\rangle = c[0,0,0,0,0,1,-1,0,0,0,0,1,1,-1,-1,1,1,-1,-1]^{\mathrm{T}}. \end{cases} \tag{9}$$

The corresponding second moment is

$$\sum_{\alpha=0}^{Q-1} \vec{e}_\alpha \otimes \vec{e}_\alpha \left(f_\alpha^{\mathrm{MHD(eq)}} - f_\alpha^{\mathrm{eq}}\right) = \frac{5C_B - 1}{2\mu}\left(\vec{B}\cdot\vec{B}\right)\mathbf{I} - \frac{1}{\mu}\vec{B}\otimes\vec{B}, \tag{10}$$

which recovers the Maxwell stress tensor only if $C_B = 2/5$ (not $C_B = 1/2$ [20]). This is the same model constant required in the D3Q27 model to recover the Maxwell stress tensor.

Note that the following properties

$$\sum_{\alpha=0}^{Q-1} \vec{e}_\alpha \left(f_\alpha^{\mathrm{MHD(eq)}} - f_\alpha^{\mathrm{eq}}\right) = 0,$$

$$\sum_{\alpha=0}^{Q-1} \vec{e}_\alpha \otimes \vec{e}_\alpha \otimes \vec{e}_\alpha \left(f_\alpha^{\mathrm{MHD(eq)}} - f_\alpha^{\mathrm{eq}}\right) = 0,$$

hold for the first and third moments, respectively, of the D2Q9, D3Q27, and D3Q19 models with arbitrary C_B due to symmetry.

3. Satisfying mass conservation

Additionally, the mass conservation law requires $\sum_{\alpha=0}^{Q-1}\left(f_\alpha^{\mathrm{MHD(eq)}} - f_\alpha^{\mathrm{eq}}\right) = 0$.

For the D2Q9 model, we have

$$\begin{aligned} \sum_{\alpha=0}^{Q-1}\left(f_\alpha^{\mathrm{MHD(eq)}} - f_\alpha^{\mathrm{eq}}\right) &= \sum_{\alpha=0}^{Q-1} \frac{\omega_\alpha}{2c_s^4\mu}\left[C_B\left(\vec{B}\cdot\vec{B}\right)\left(\vec{e}_\alpha\cdot\vec{e}_\alpha\right) - \left(\vec{e}_\alpha\cdot\vec{B}\right)^2\right] \\ &\propto C_B\left(\vec{B}\cdot\vec{B}\right)c^2\left(0 + \frac{1\times4\times1}{9} + \frac{1\times4\times2}{36}\right) - \frac{c^2}{3}\left(\vec{B}\cdot\vec{B}\right) \propto \left(\frac{2C_B}{3} - \frac{1}{3}\right), \end{aligned} \tag{11}$$

which is zero only if $C_B = 1/2$. This is the same model constant required to recover the Maxwell stress tensor.

For both the D3Q19 and D3Q27 models, we have

$$\sum_{\alpha=0}^{Q-1}\left(f_\alpha^{\mathrm{MHD(eq)}} - f_\alpha^{\mathrm{eq}}\right) \propto C_B - \frac{1}{3}, \tag{12}$$

which is zero only if $C_B = 1/3$. This is different from the value of $2/5$ required to recover the Maxwell stress tensor. Using $C_B = 1/3$ for the D3Q19 and D3Q27 models to maintain mass conservation was also reported in Refs. [21, 22, 23], but fails to recover the correct Maxwell stress tensor due to Eqs. (8) and (10).

4. A consistent 3D model for the equilibrium distribution function

To eliminate the inconsistencies discussed above, an additional term can be added to Eq. (1), as proposed in Refs. [25, 26], as follows

$$f_\alpha^{\mathrm{MHD(eq)}} = f_\alpha^{\mathrm{eq}} + \frac{\omega_\alpha}{2c_s^4\mu}\left[\frac{1}{2}\left(\vec{B}\cdot\vec{B}\right)(\vec{e}_\alpha\cdot\vec{e}_\alpha) - \left(\vec{e}_\alpha\cdot\vec{B}\right)^2 - \frac{c^2}{6}\left(\vec{B}\cdot\vec{B}\right)\right]. \tag{13}$$

It may be verified that for the D3Q15, D3Q19, and D3Q27 models, the Maxwell stress tensor is recovered exactly, and we have the zeroth moment equal to zero for mass conservation. Additionally, the first moment is also equal to zero for momentum conservation, and the third moment is equal to zero for high-order accuracy. Therefore, it is recommended that this modification be used in three-dimensional simulations. For ease of reference, the model above is henceforth referred to as the “consistent model”.

Note that modifying f_α^{eq} is also used to recover the desired bulk viscosity term in the stress tensor while keeping the zeroth, first, and third moments of f_α^{eq} unchanged, as examined in Ref. [27].

5. Results and Discussion

While the inconsistent models discussed above may not have generated significant errors in particular set-ups, such as in those previously investigated by the 3D LBM-MHD studies of Refs. [19, 20, 21, 22, 23, 24], such mismatches in the moments of the equilibrium distribution function can have noticeable influence in more general scenarios. To systematically investigate these potential consequences of model inconsistencies, we have focused our discussion on specific set-ups where such inconsistencies are expected to manifest errors of significant impact. Three different categories of flow problems are simulated and quantitatively analysed to cover common scenarios in practical applications. The set-up for each category is simplified to enable general theoretical analysis, with the intention for the conclusions about the models’ consistency to be generalisable to more complex set-ups and geometries. Using $C_B \neq 1/3$, as was done in Refs. [19, 20, 24], violates mass conservation. This can lead to both unphysical results in open problems and remarkable errors in closed problems, as we will show in Sections 5.1 and 5.2, respectively. When $C_B = 1/3$ is used to conserve mass without the extra model term, as adopted in Refs. [21, 22, 23], the mismatch in recovering the Maxwell stress tensor affects the magnetic pressure term. This can cause noticeable errors when the magnetic pressure gradient plays an important role in driving the flow, as we show in Section 5.3.

We consider three variations of Hunt’s flow in a rectangular channel and perform 3D LBM MHD simulations with the consistent and inconsistent models. Schematics of the three cases to be considered, including the domain set-up and boundary conditions for the magnetic field, velocity, and pressure, are illustrated in Fig. 1. Variables and constants are hereinafter expressed in SI units, which can be numerically realised by adopting the appropriate Δx and $c = \Delta x/\Delta t$ in the formulation. The corresponding dimensionless parameters are summarised in Table 1 for each case.

Dimensionless parameter	Case 1	Case 2	Case 3
Reynolds number $Re = u_{1,\max}L_2/\nu$	2.6	0.20	0.15
Magnetic Reynolds number $Re_m = \mu\sigma u_{1,\max}L_2$	2.6	0.20	0.15
Magnetic Prandtl number $Pr_m = \nu\mu\sigma$	1.0	1.0	1.0
Hartmann number $Ha = B_{\mathrm{ext},2}L_2\sqrt{\sigma/\mu}/2$	4.0	4.0	4.0

Table 1: Dimensionless parameters for the cases considered in this work. The field strength used for the Hartmann number of Case 3 is its maximum value in the domain. L_2 is the length of the domain in the x_2 direction.

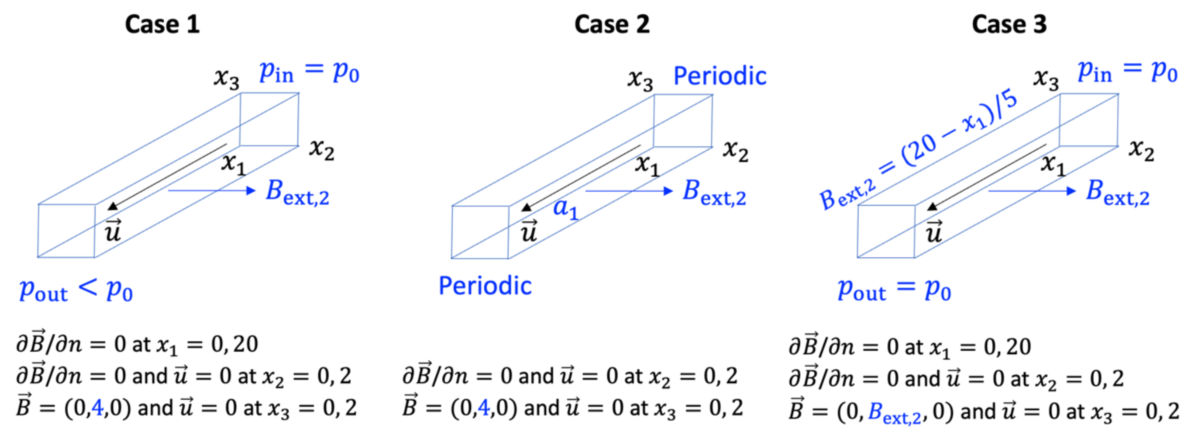

Fig. 1: Schematics of Hunt's flow and its variants considered in this work.

5.1. Case 1: Hunt's flow in an open channel

In Case 1, a Hunt's flow simulation is driven in the x_1 direction of a rectangular channel with a domain size of $20 \times 2 \times 2$ using a pressure difference, namely by having $p_{\text{in}} = p_0 = \rho_0 c^2/3$ at $x_1 = 0$ and $p_{\text{out}} = 0.98\rho_0 c^2/3 < p_0$ at $x_1 = 20$. The boundary conditions for the magnetic field, $\vec{B}$, are $\partial\vec{B}/\partial n = 0$ for the conducting walls at $x_2 = 0$ and 2, as well as for the inlet and outlet; and $\vec{B} = \vec{B}_{\text{ext}} = (0, B_{\text{ext},2}, 0)$ for the insulating walls at $x_3 = 0$ and 2. At the walls with $\vec{u} = 0$, the halfway bounce-back scheme is used for the no-slip velocity boundary condition. The magnetic boundary condition is implemented by the halfway bounce-back scheme for $\partial\vec{B}/\partial n = 0$ and the halfway anti-bounce-back scheme for $\vec{B} = \vec{B}_{\text{ext}}$ [28]. At the open boundaries, the non-equilibrium extrapolation scheme [29] is used to enforce fixed densities and pressures, while the vector-valued distribution function used for solving $\vec{B}$ is retrieved from the corresponding neighbouring grid cell in the normal direction located inside the computational domain, which imposes $\partial\vec{B}/\partial n = 0$ regardless of $\vec{u}$.

An external magnetic field of $B_{\text{ext},2} = 4$ is imposed in the x_2 direction. For simplicity of normalisation and discussion, we have selected the following fluid parameters: $\rho_0 = 1$ for the reference density, $\sigma = 1$ for the electrical conductivity, $\nu = 1$ for the kinematic viscosity, and $\mu = 1$ for the magnetic permeability. Extension of our formulation to non-unity parameters is straightforward. A baseline grid-cell count of $400 \times 40 \times 40$ (in addition to an extra grid layer inside each solid wall used to implement the halfway bounce-back scheme) is used in the LBM simulations. The grid-cell-to-time-step ratio $c = \Delta x/\Delta t = 10/\Delta x$ is used such that $\nu = c\Delta x(\tau - 0.5)/3 = 1$ holds at a fixed relaxation time $\tau = 0.8$ for the flow solver.

We compare simulations using the consistent model of Eq. (13) and the inconsistent models of Eq. (1) with $C_B = 1/2$ and 1. Fig. 2 shows the density variation along the driving direction, x_1. The density in Fig. 2(a), obtained from the consistent model, varies from 1 at the inlet to 0.98 at the outlet as expected. However, the density variation has a peak at the channel centre when the inconsistent models are used. Due to the violation of mass conservation in the inconsistent models, the relative error in mass, $\sum_{\alpha=0}^{Q-1}\left(f_\alpha^{\text{MHD(eq)}} - f_\alpha^{\text{eq}}\right)/\sum_{\alpha=0}^{Q-1} f_\alpha^{\text{eq}}$, is 0.03% for $C_B = 1/2$ and 0.12% for $C_B = 1$. Although these errors are relatively small, they are compounded in *all* grid points over *every* time step via the collision process. While there is a depletion effect at open boundaries with fixed or lower densities, this depletion is much slower than the error compounding, particularly in the domain interior.

After long-time advancement, a balance is achieved with a sharply decreasing density from the centre towards the open boundaries, as shown in Fig. 2(b) and (c). The peak value associated with $C_B = 1$ is higher than that associated with $C_B = 1/2$ because the former has a larger relative error in mass conservation. Additionally, the density variation of the inconsistent models is almost symmetric in x_1 because the small difference of 2% in the imposed densities at the two ends is negligible relative to the density variation resulting from the violation of mass conservation.

The unphysical density variations obtained by the inconsistent models lead to unphysical pressure variations that drive the flow from the channel centre towards the two ends. Fig. 3(a) shows the variation in streamwise velocity, u_1, at the mid-plane, as obtained from the consistent model. The inconsistent models result in completely different velocity profiles, as evidenced in Fig. 3(b) and (c). Similarly, the spatial distributions of the streamwise induced magnetic field, B_1, obtained by the inconsistent models are completely different from the corresponding distribution of the consistent model, as shown in Fig. 4. Note that the unphysical flow pattern obtained from the inconsistent model will also occur in other open problems where the pressure is fixed at the inlet(s) and/or outlet(s), since the internal pressure will accumulate due to the violation of mass conservation.

We do not observe significant differences between the consistent model and the inconsistent model using $C_B = 1/3$, which conserves mass. This is because the magnetic field $\vec{B}$ and magnetic pressure $B^2/(2\mu)$ do not change along the driving direction and the error in magnetic pressure does not manifest. The corresponding comparison is omitted.

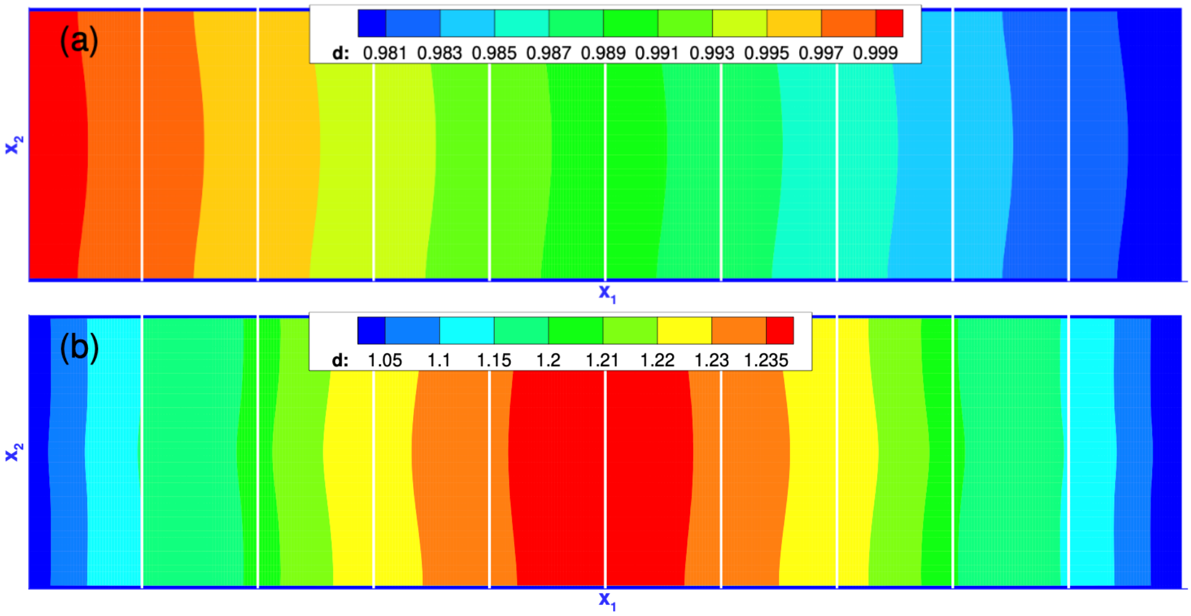

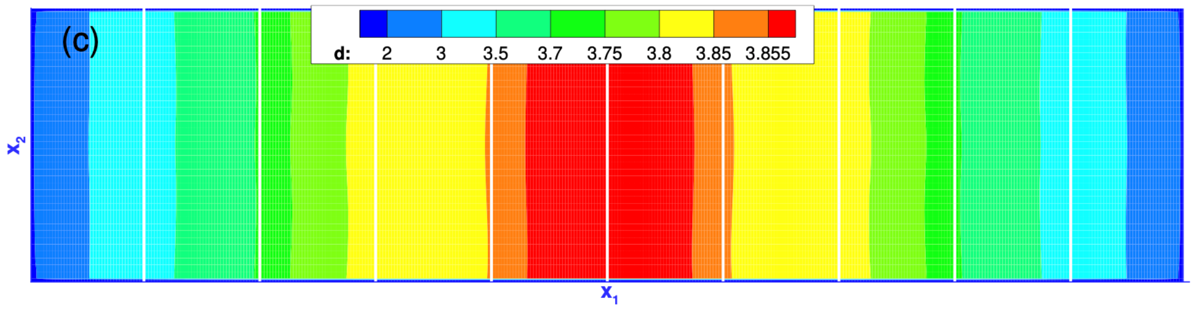

Fig. 2: Spatial variation of the density $d \equiv \rho$ on the middle plane at $x_3 = 1$ obtained using (a) the consistent model [25, 26], as well as the inconsistent models with (b) $C_B = 1/2$ [19, 20] and (c) $C_B = 1$ [24]. The white vertical lines denote the domain decomposition boundaries in our parallel simulation and may be neglected. Note the difference in colour bar ranges in the three panels.

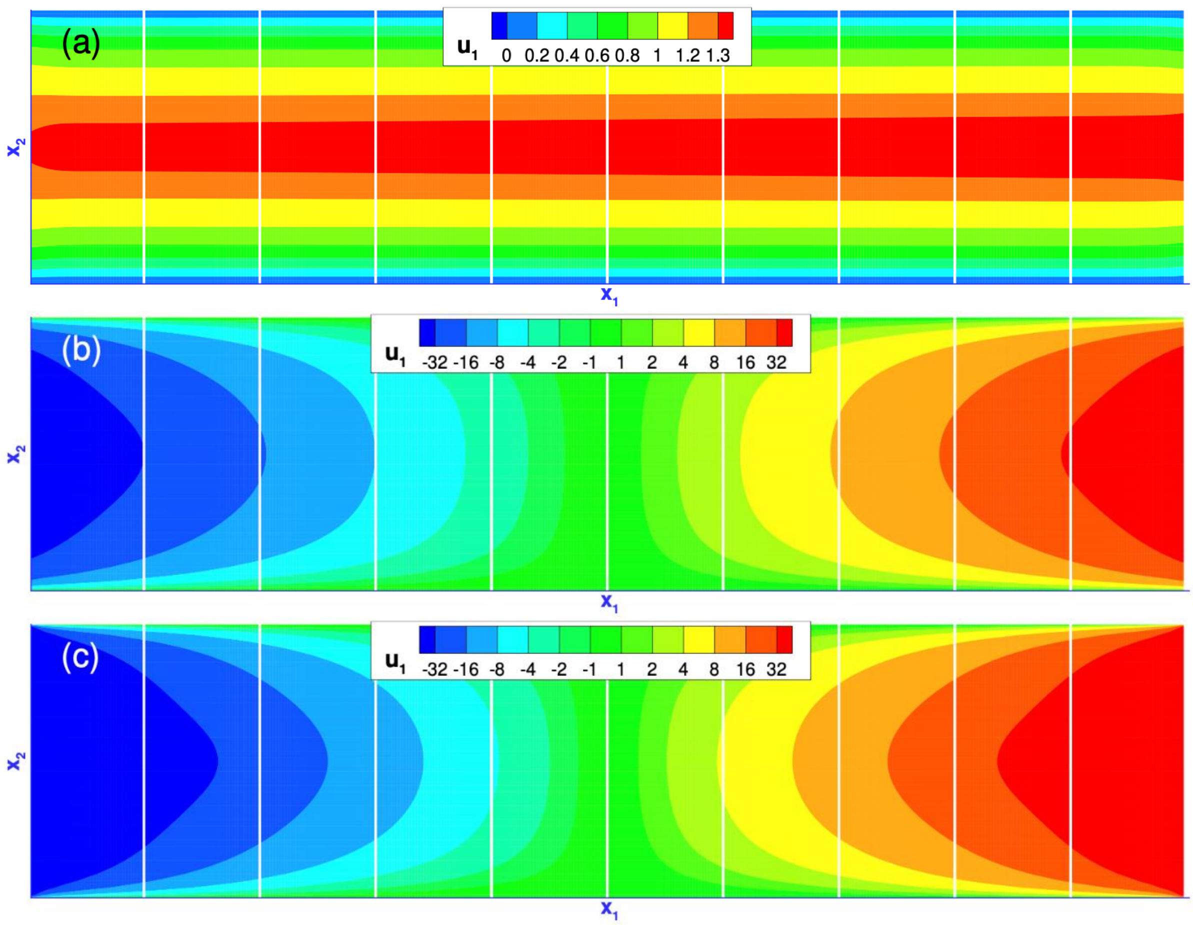

Fig. 3: Spatial variation of the streamwise (x_1) velocity u_1 on the middle plane at $x_3 = 1$ obtained using (a) the consistent model [25, 26], as well as the inconsistent models with (b) $C_B = 1/2$ [19, 20] and (c) $C_B = 1$ [24]. Note the difference in colour bar ranges between the top panel and the other two panels.

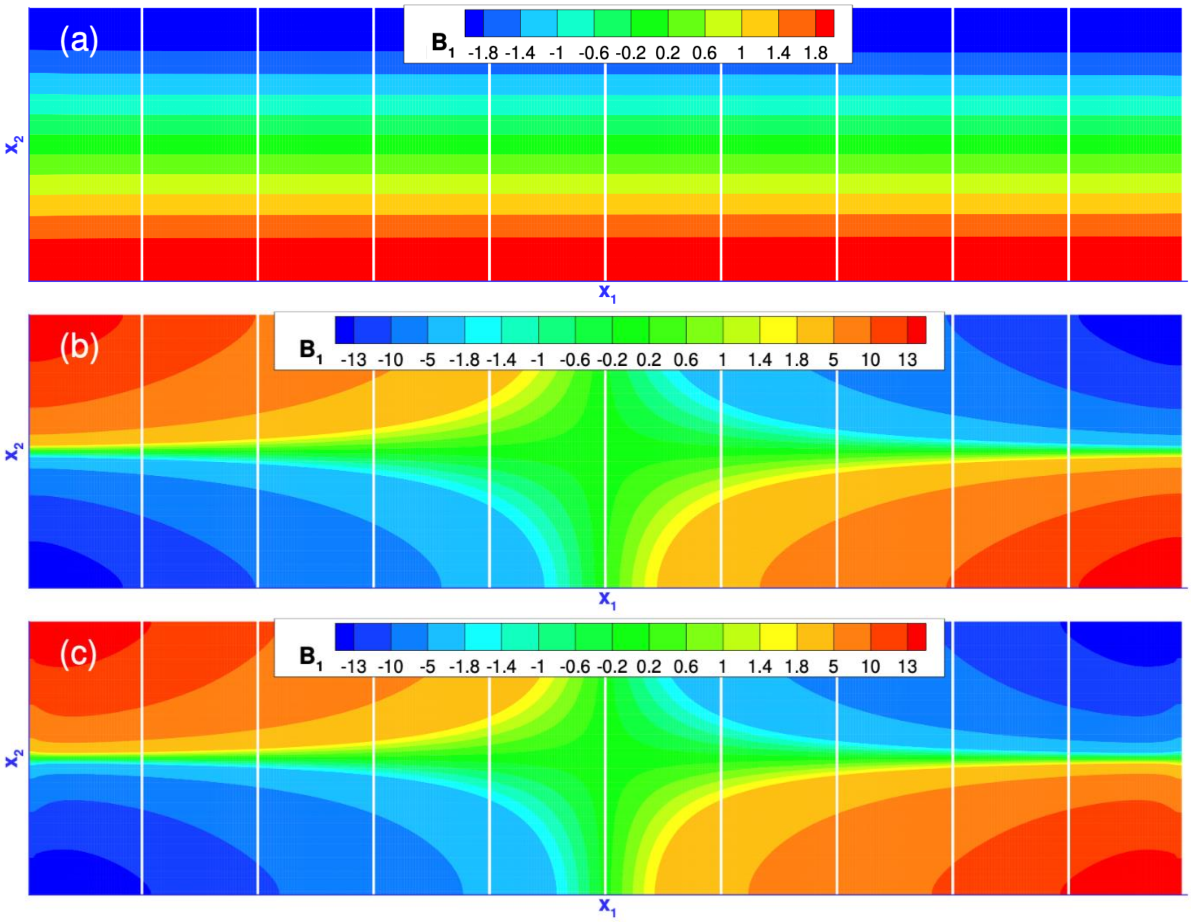

Fig. 4: Spatial variation of the streamwise induced magnetic field, B_1, on the middle plane at $x_3 = 1$ obtained using (a) the consistent model [25, 26], as well as the inconsistent models with (b) $C_B = 1/2$ [19, 20] and (c) $C_B = 1$ [24]. Note the difference in colour bar ranges between the top panel and the other two panels.

5.2. Case 2: Hunt's flow in a closed channel

In Case 2, the previous Hunt's flow is simulated again but with the flow now driven by an external body force a_1 per unit mass, with $a_1 = 1$ in the current study. Correspondingly, the previous inlet and outlet boundaries are replaced by periodic boundaries. The external force is implemented using the exact difference method [30] and the flow velocity in the x_1 direction, u_1, is computed with an additional force term $0.5\Delta t a_1$. To reduce computational cost, only 5 grid points are used in the driving direction in this case, but the channel cross-section is still resolved by 40×40 grid points. For comparison with the analytical solution [31], the obtained velocity and magnetic field are divided by the external force $\rho_0 a_1$.

The spatial profiles of u_1 and B_1 are plotted in Fig. 5(a)–(c), which show good agreement between the consistent model of Eq. (13) and the analytical solutions. Although the inconsistent models of Eq. (1) with $C_B = 1/2$ and 1 have the correct profile shapes as seen in Fig. 5(e)–(h), the magnitudes of the obtained u_1 and B_1 increase with time. The reason is that the mass conservation violation continuously increases the density ρ, since there is erroneous mass replenishment but no mass depletion in closed problems. Consequently, the body force ρa_1 per unit volume increases with time. Assuming that the velocity solution u_1 is unchanged, the viscous friction $\rho \nu \Delta u_1$ will increase proportionally to ρa_1, while the magnetic component of the Lorentz force, $\vec{J} \times \vec{B} = \left(\mu^{-1} \nabla \times \vec{B}\right) \times \vec{B}$, remains unchanged like u_1 according to Eq. (2). This implies that the driving force ρa_1 becomes larger than the total drag forces of $\rho\nu\Delta u_1$ and $\left(\vec{J} \times \vec{B}\right)_1$. Therefore, a balance of forces requires u_1 to increase with ρ, and $|B_1|$ increases as well. The increase in total mass, namely ρ, with time using the inconsistent models is also shown in Fig. 5(d).

As with Case 1, we do not observe significant differences between the consistent model and the mass-conserving inconsistent model with $C_B = 1/3$, and the corresponding comparison is omitted.

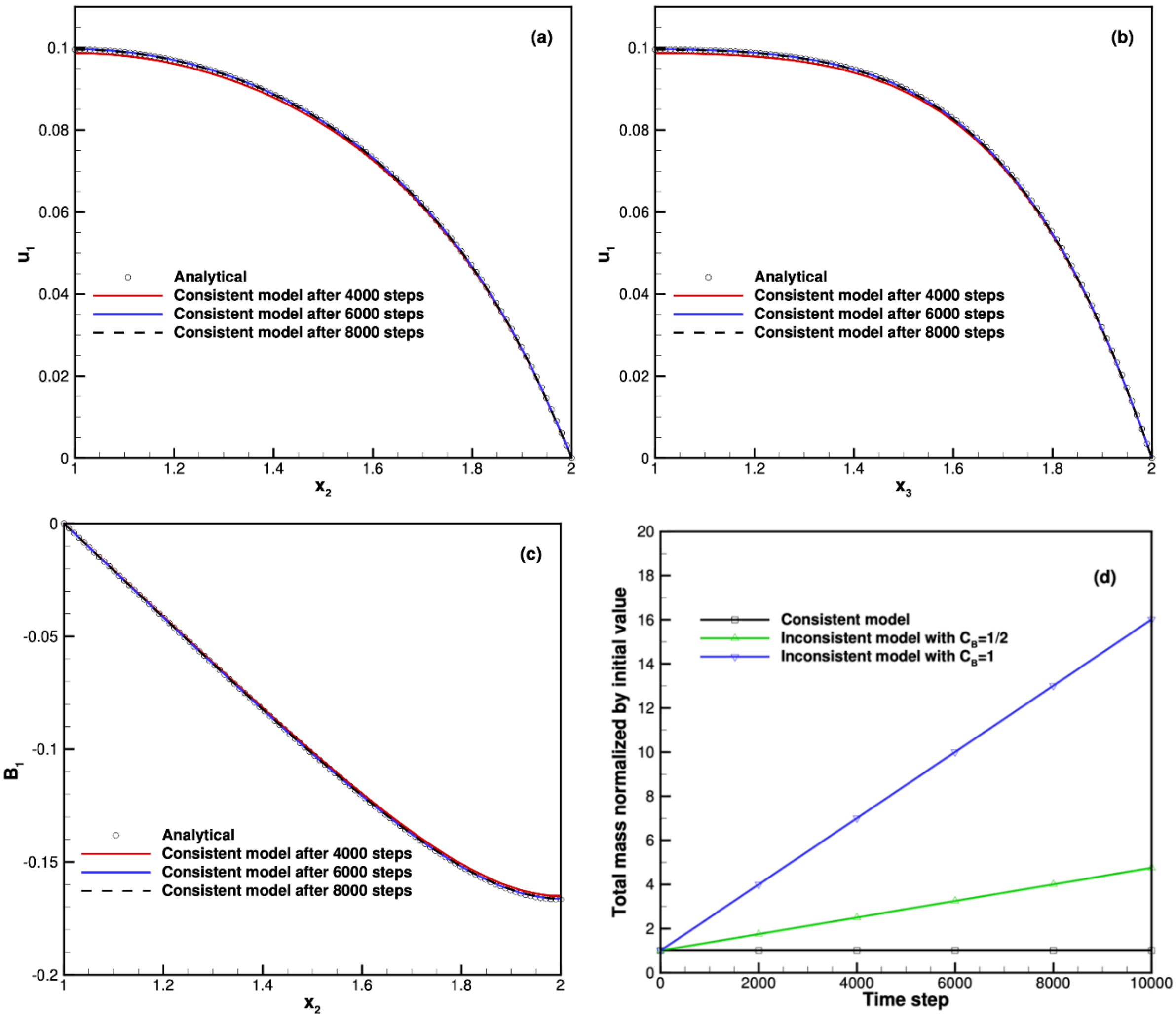

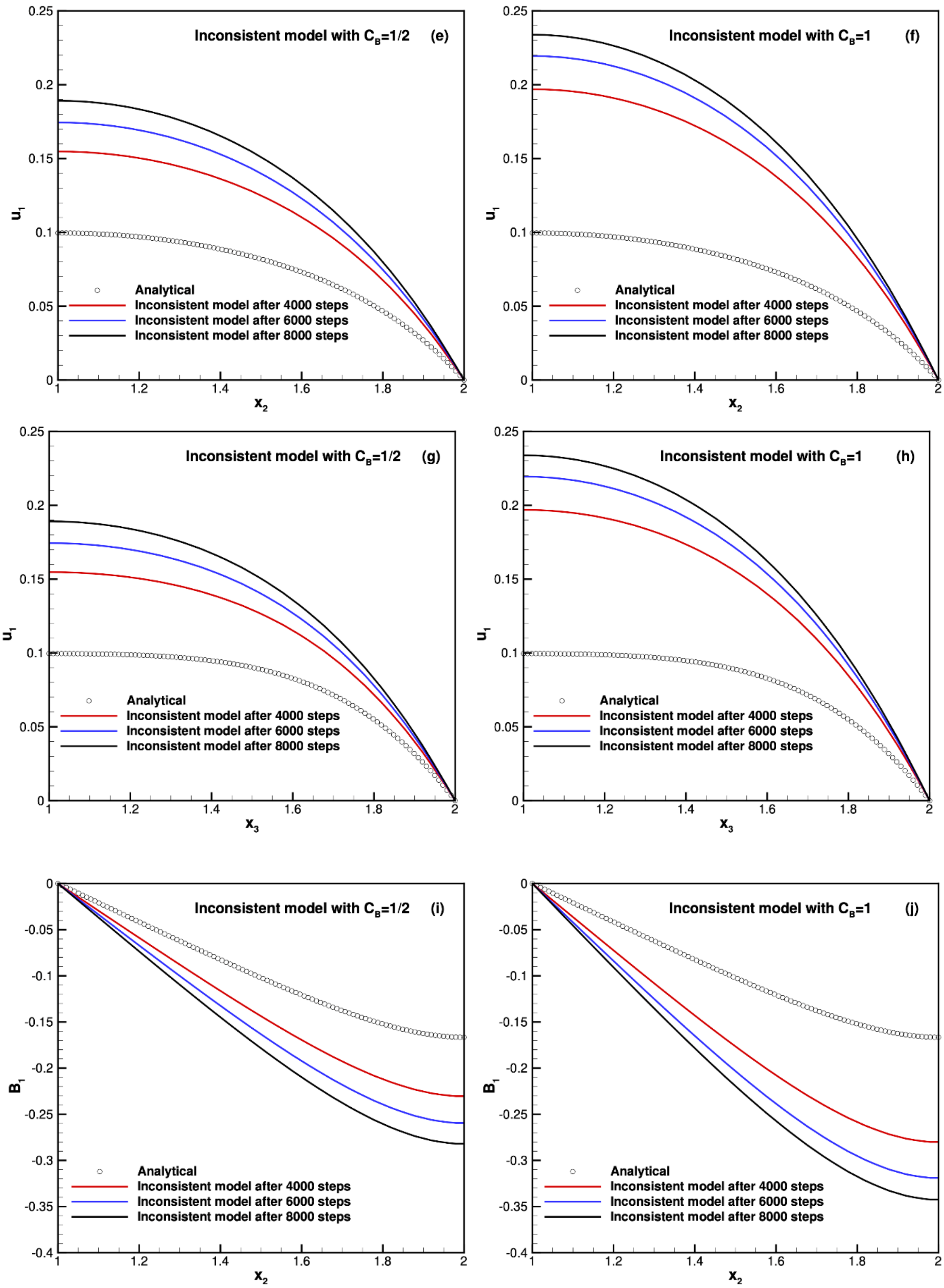

Fig. 5: Comparison of (a–c) the consistent model [25, 26], as well as the inconsistent models using (e,g,i) $C_B = 1/2$ [19, 20] and (f,h,j) $C_B = 1$ [24], with analytical solutions [31] for (a,b,e–h) u_1 and (c,i,j) B_1, and (d) with one another for ρ. Only half of each profile, which is symmetric with respect to either $x_2 = 1$ or $x_3 = 1$, is plotted. All spatial profiles are plotted with respect to x_2 except panels (b), (g), and (h), which are plotted with respect to x_3. The time step size is $\Delta t = \Delta x / c = \Delta x^2/10 = 1/4000$.

Based on results from the consistent model in Fig. 5(a)–(c), we note that, physically, the solutions are reasonably converged after $t = 4000\Delta t$. Therefore, the evolution/deviation of the magnetic field and velocity profiles in the inconsistent models after this time instant results from error accumulation (i.e., 0.03% of the instantaneous speed for $C_B = 1/2$ and 0.12% of the instantaneous speed for $C_B = 1$ per time step). The speed is therefore reported as a function of the number of elapsed time steps (i.e., iterations) rather than the physical time. The time step size, Δt, is provided in the figure caption for clarity.

In Fig. 6, we focus on the physical convergence process using the consistent model with different $\tau, c, \Delta t$, and correspondingly different relaxation times τ_g for the magnetic field solver. Hence, the results are presented at fixed physical times instead of a fixed number of elapsed time steps. As before, the channel cross-section is resolved with 40×40 grid points and $\Delta x = 1/20$. Unlike the baseline set-up ($\tau = 0.8$ and $c = 10/\Delta x$ to match $\nu \equiv c\Delta x(\tau - 0.5)/3 = 1$), we adjust c here for arbitrary τ according to $c \equiv 3\nu/[\Delta x(\tau - 0.5)]$. Furthermore, the relation $\tau_g \equiv 0.5 + 4/(\mu\sigma c\Delta x)$ indicates that τ_g changes with τ via c. Keeping $\nu = \mu = \sigma = 1$ and $\Delta x = 1/20$, we have $c = 60/(\tau - 0.5)$ and $\tau_g = 0.5 + 4(\tau - 0.5)/3$ when varying τ for a parametric study. In Fig. 6, we consider $\tau = 0.6, 0.7$, and 0.9. We find that the transient results obtained using different $\tau, c, \Delta t, \tau_g$ at the same physical time are essentially identical, demonstrating the parameter-independent property of the solvers. Additionally, all results converge to the analytical solutions after about 1 second of physical time, as further demonstrated by convergence in subsequent snapshots (not shown here).

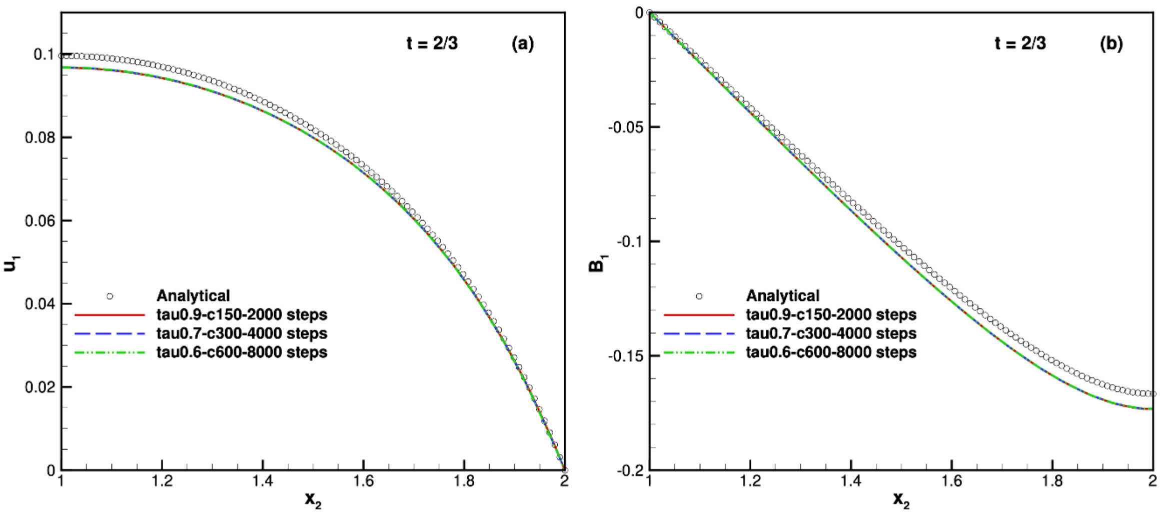

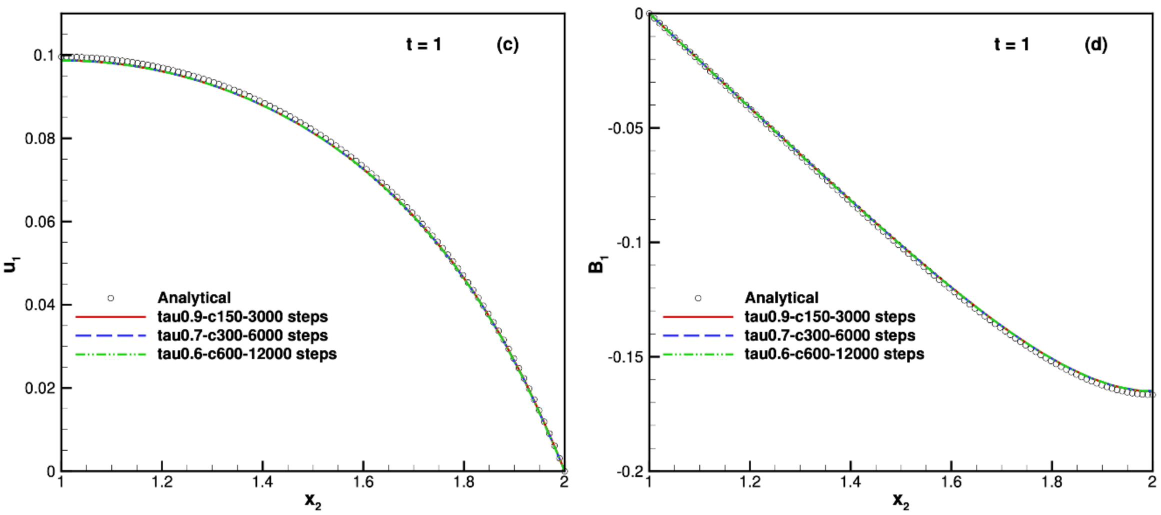

Fig. 6: Simulations with different values of $\tau, c, \Delta t$, and $\tau_g = 0.5 + 4(\tau - 0.5)/3$ in the consistent model [25, 26]. The dash-dotted green, dashed blue, and solid red curves correspond to $\tau = 0.6, 0.7,$ and 0.9, respectively. Reasonable agreement across the parameters demonstrates that the solvers are parameter independent.

5.3. Case 3: Flow driven by a difference of magnetic pressure in an open channel

In Case 3, we adopt the previous set-up of Section 5.1 with two open boundaries (Case 1), but we impose the same density $\rho_0 = 1$ at the two ends. The corresponding difference in thermodynamic pressure is zero. The boundary conditions for the magnetic field $\vec{B}$ are $\partial\vec{B}/\partial n = 0$ for the conducting walls at $x_2 = 0$ and 2, as well as for the inlet and outlet. Additionally, instead of using a constant $B_{\text{ext},2} = 4$ in $\vec{B} = \vec{B}_{\text{ext}} = (0, B_{\text{ext},2}, 0)$ for the walls at $x_3 = 0$ and 2, we apply a linear variation in the imposed field strength along x_1, such that $B_{\text{ext},2} = 4(L_1 - x_1)/L_1$, where $L_1 = 20$ is the channel length. The top and bottom walls, which are conducting, have an electric current $J_3 < 0$, which drives the flow in the x_1 direction as $\left(\vec{J} \times \vec{B}\right)_1 \approx -J_3 B_2 > 0$.

Throughout the computational domain, the obtained density and thermodynamic pressure are almost uniform (plots omitted here). The flow is mainly driven by the magnetic component of the Lorentz force, $\vec{J} \times \vec{B} = \mu^{-1}\nabla \cdot \left(-\frac{1}{2}B^2\mathbf{I} + \vec{B}\otimes\vec{B}\right)$. Note that the induced B_3 is almost zero, and B_1 is much smaller than B_2 as shown in Fig. 7 and Fig. 8. The magnitude of the induced B_1 decreases with an increase in x_1 as the imposed $B_{\text{ext},2}$ does. For the x_1 magnetic component of the Lorentz force, the first term corresponding to the gradient of magnetic pressure is $-\frac{1}{2\mu}\partial_{x_1}(B^2) \propto B_2^2$, which is the driving force of the flow. The second term, $\mu^{-1}\vec{B} \cdot \nabla B_1 \propto B_2 B_1$, corresponds to a drag force. The first term is much larger than the second term since $B_2 \gg B_1$. When the inconsistent model with $C_B = 1/3$ is used, the magnetic pressure changes from $\frac{1}{2\mu}B^2$ to $\frac{1}{3\mu}B^2$ [see Eqs. (8) and (10)], which can be balanced if both the drag force $\mu^{-1}\vec{B} \cdot \nabla B_1$ and the viscous friction $\rho\nu\Delta u_1$ are also decreased by a factor of 2/3. This is exactly what is observed in the comparisons of Fig. 7–Fig. 9, where $B_2 \approx B$ is almost unchanged while B_1 and u_1 are decreased by a factor of 2/3. Therefore, noticeable errors will occur when using the inconsistent model with $C_B = 1/3$ if the magnetic pressure plays an important role in driving the flow.

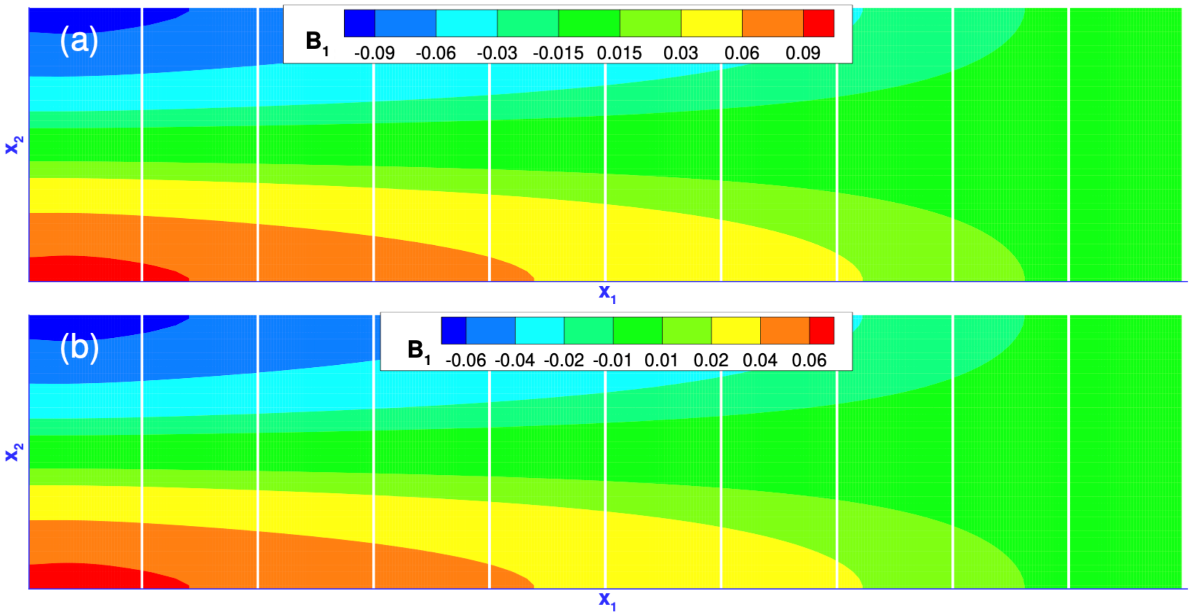

Fig. 7: Spatial variation of the streamwise induced magnetic field, B_1, on the middle plane at $x_3 = 1$ obtained using (a) the consistent model [25, 26] and (b) the inconsistent model with $C_B = 1/3$ [21, 22, 23]. Note the difference in colour bar ranges in the two panels.

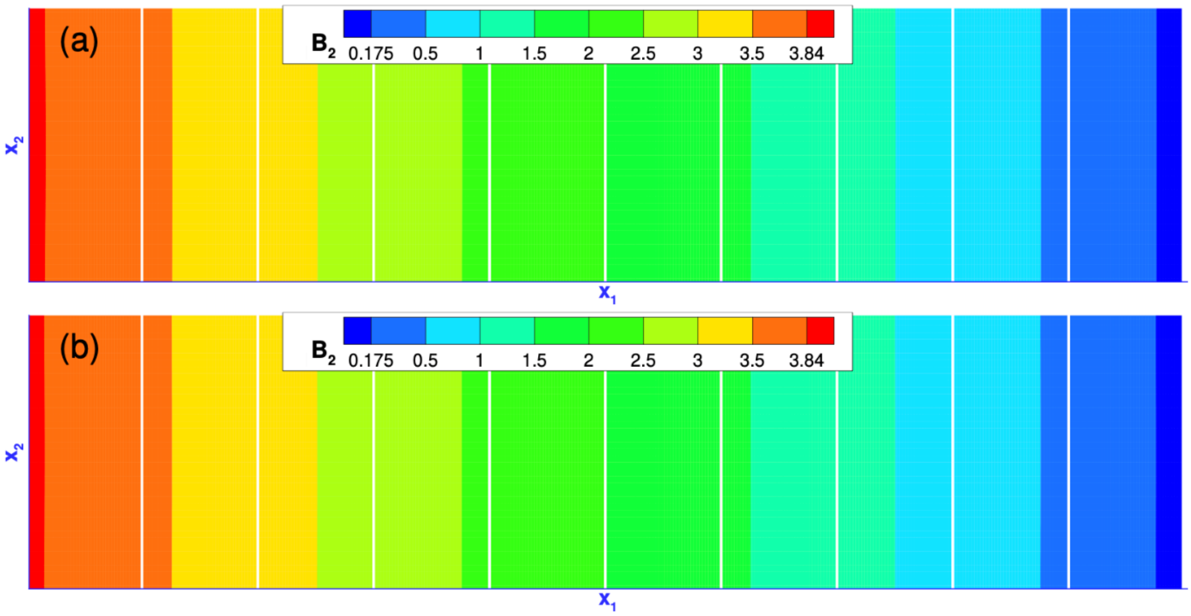

Fig. 8: Spatial variation of the x_2 component of the magnetic field, B_2, including its imposed and induced contributions, on the middle plane at $x_3 = 1$ obtained using (a) the consistent model [25, 26] and (b) the inconsistent model with $C_B = 1/3$ [21, 22, 23]. There is negligible difference between the two solutions.

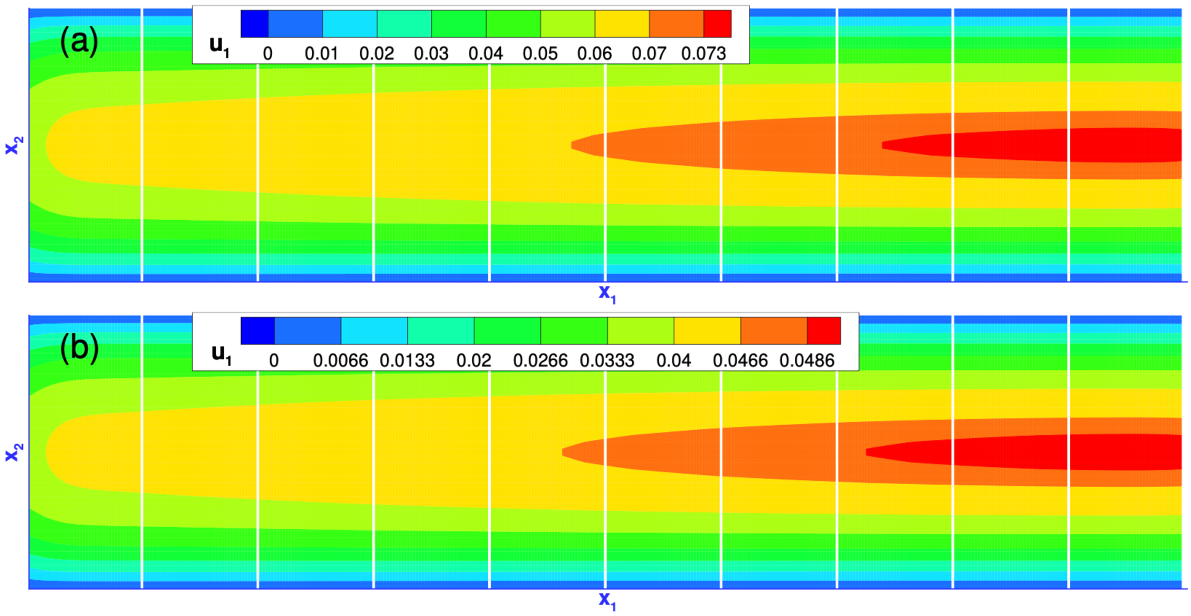

Fig. 9: Spatial variation of the streamwise velocity, u_1, on the middle plane at $x_3 = 1$ obtained using (a) the consistent model [25, 26] and (b) the inconsistent model with $C_B = 1/3$ [21, 22, 23]. Note the difference in colour bar ranges in the two panels.

6. Conclusions

We investigated different 3D LBM models for MHD flows that modify the equilibrium distribution function of the flow solver to recover the Maxwell stress tensor, as proposed in the original 2D model to incorporate the Lorentz force. Most 3D models adopt one free parameter C_B, which cannot simultaneously recover the Maxwell stress tensor and conserve mass exactly. The violation of mass conservation by using $C_B \neq 1/3$ could lead to unphysical results and significant errors in simulating open and closed problems, respectively. Using $C_B = 1/3$ can conserve mass and the obtained solutions are accurate in problems where the magnetic pressure is uniform. However, there is a mismatch in the magnetic pressure when using $C_B = 1/3$. We show that noticeable errors can occur if the magnetic pressure gradient plays an important role in driving the flow of interest. On the other hand, a consistent 3D model that incorporates an additional term has been previously proposed, albeit without widespread uptake, and can simultaneously satisfy the two requirements discussed above. We show that its simulation results agree very well with the analytical solutions in a representative reference problem. The extended 3D model is simple to implement, does not cause significant increase in computational cost, and is broadly recommended for 3D MHD simulations due to its theoretical consistency and simplicity for practical implementations.

It is worth noting that the Lorentz force can also be directly implemented through a force model [12, 23, 28, 32] without consistency issues, as an alternative to modifying the equilibrium distribution function as studied in the current work. A performance comparison between these two approaches is deferred to future work.

Acknowledgements

The authors would like to thank Valerian Hall-Chen, Frank Meng, and Andrei Khodak for their input to an MHD modelling problem that inspired this work. We also thank the anonymous reviewers for their careful reading of our manuscript and for their insightful comments.

Appendix

The detailed algorithms of solving the flow and the magnetic field are provided here for completeness. The scalar distribution function, f_α, is used for the flow simulation and evolves according to a relaxation–propagation process

$$f_\alpha(\vec{x}+\vec{e}_\alpha\Delta t, t+\Delta t) = f_\alpha(\vec{x},t) + \frac{f_\alpha^{\mathrm{MHD(eq)}}(\vec{x},t) - f_\alpha(\vec{x},t)}{\tau}, \quad \text{(A1)}$$

where $f_\alpha^{\mathrm{MHD(eq)}}$ is modified from f_α^{eq} using $\vec{B}$ via Eq. (1), and f_α^{eq} is computed from the density $\rho = \sum_{\alpha=0}^{Q-1} f_\alpha$ and the velocity $\vec{U} = (1/\rho)\sum_{\alpha=0}^{Q-1} \vec{e}_\alpha f_\alpha$ as follows

$$f_\alpha^{\mathrm{eq}}(\rho,\vec{U}) = \rho\omega_\alpha\left[1 + \frac{3}{c^2}\vec{e}_\alpha\cdot\vec{U} + \frac{9}{2c^4}\left(\vec{e}_\alpha\cdot\vec{U}\right)^2 - \frac{3}{2c^2}\vec{U}\cdot\vec{U}\right]. \quad \text{(A2)}$$

The relaxation time τ is selected to match the kinematic viscosity $\nu = c\Delta x(\tau - 0.5)/3$. The D3Q19 lattice model is used to determine ω_α and $\vec{e}_\alpha$. The thermodynamic pressure p is computed as $p = \rho c^2/3$ and imposed at open boundaries by fixing ρ in the non-equilibrium extrapolation scheme [29]. The halfway bounce-back scheme of f_α is used for the no-slip velocity boundary condition. The computed $\vec{U}$ is the flow velocity $\vec{u}$ in the absence of other force sources different from the Lorentz force.

For problems with an extra body force $\vec{a}$ per unit mass, such as in Case 2, an additional term $\Delta f_\alpha(\vec{x},t)$ is added to the right-hand side of Eq. (A1) by using the exact difference method [30]

$$\Delta f_\alpha = f_\alpha^{\mathrm{eq}}\left(\rho,\vec{U}+\Delta t\vec{a}\right) - f_\alpha^{\mathrm{eq}}\left(\rho,\vec{U}\right). \quad \text{(A3)}$$

Correspondingly, the flow velocity becomes $\vec{u} = \vec{U} + 0.5\Delta t\vec{a}$. Note that f_α^{eq} is used only to compute Δf_α and $f_\alpha^{\mathrm{MHD(eq)}}$. The full $f_\alpha^{\mathrm{MHD(eq)}}$ is used throughout the code.

The magnetic field $\vec{B}$ governed by Eq. (2) is modelled separately by a vector-valued distribution function $\vec{g}_\alpha$, which evolves as follows [18]

$$\vec{g}_\alpha\left(\vec{x}+\vec{\xi}_\alpha\Delta t, t+\Delta t\right) = \vec{g}_\alpha^{\mathrm{rel}}(\vec{x},t) = \vec{g}_\alpha(\vec{x},t) + \frac{\vec{g}_\alpha^{\mathrm{eq}}(\vec{x},t) - \vec{g}_\alpha(\vec{x},t)}{\tau_g}, \quad \text{(A4)}$$

where $\vec{g}_\alpha^{\mathrm{eq}}$ is computed from $\vec{B} = \sum_{\alpha=0}^{M-1}\vec{g}_\alpha$ and the flow velocity $\vec{u}$

$$\vec{g}_\alpha^{\mathrm{eq}}(\vec{B},\vec{u}) = \varpi_\alpha\left[\vec{B} + \frac{1}{c_g^2}\vec{\xi}_\alpha\cdot\left(\vec{u}\otimes\vec{B} - \vec{B}\otimes\vec{u}\right)\right]. \quad \text{(A5)}$$

Although there is no physical analogy to justify using a kinetic model for $\vec{B}$, the developed LBM algorithm can be taken as a numerical solver of the magnetic induction equation (2) in a kinetic form that has numerical advantages. The relaxation time τ_g is selected to match the magnetic diffusivity/resistivity $\eta = 1/(\mu\sigma) = (\tau_g - 0.5)c_g^2\Delta t$. The D3M7 lattice model [21] with $c_g = c/2$ is used to determine another set of the weight factors ϖ_α and lattice velocities $\vec{\xi}_\alpha$ in the $\alpha \in [0, M-1]$ directions. The constraints of such a model selection are $\sum_{\alpha=0}^{M-1}\varpi_\alpha = 1$ and $\sum_{\alpha=0}^{M-1}\varpi_\alpha\xi_{\alpha i}\xi_{\alpha j} = c_g^2\delta_{ij}$, in addition to the symmetry requirements

$\sum_{\alpha=0}^{M-1} \varpi_\alpha \xi_{\alpha i} = 0$ and $\sum_{\alpha=0}^{M-1} \varpi_\alpha \xi_{\alpha i} \xi_{\alpha j} \xi_{\alpha k} = 0$ up to the third order. It is easy to verify that $\sum_{\alpha=0}^{M-1} \vec{\xi}_\alpha \otimes \vec{g}_\alpha^{\mathrm{eq}} = \vec{u} \otimes \vec{B} - \vec{B} \otimes \vec{u}$, which recovers $\nabla \cdot (\vec{u} \otimes \vec{B} - \vec{B} \otimes \vec{u})$ on the left-hand side, equivalent to $\nabla \times (\vec{u} \times \vec{B})$ on the right-hand side of Eq. (2).

The components J_k of the current density $\vec{J} = \mu^{-1} \nabla \times \vec{B}$, if needed, can be computed by a local summation of the non-equilibrium distribution as follows [18]

$$J_k = \frac{1}{\mu} \epsilon_{ijk} \frac{\partial B_j}{\partial x_i} = \frac{-1}{\mu \Delta t \tau_g c_g^2} \epsilon_{ijk} \left(\Lambda_{ij} - \Lambda_{ij}^{\mathrm{eq}} \right), \tag{A6}$$

where i, j, k take all the three values 1,2,3 for the three spatial dimensions, ϵ_{ijk} is the Levi-Civita tensor, $\Lambda_{ij} = \sum_{\alpha=0}^{M-1} \xi_{\alpha i} g_{\alpha j}$, and $\Lambda_{ij}^{\mathrm{eq}} = \sum_{\alpha=0}^{M-1} \xi_{\alpha i} g_{\alpha j}^{\mathrm{eq}} = u_i B_j - B_i u_j$. Note that $g_{\alpha j}$ used in computing Λ_{ij} for J_k is the value after propagation, which is different from the value $g_{\alpha j}^{\mathrm{rel}}$ after relaxation. For the single-relaxation-time model of Eq. (A4), we have

$$g_{\alpha j}^{\mathrm{rel}} - g_{\alpha j}^{\mathrm{eq}} = \frac{\tau_g - 1}{\tau_g} \left(g_{\alpha j} - g_{\alpha j}^{\mathrm{eq}} \right), \tag{A7}$$

which indicates that a coefficient $\tau_g / (\tau_g - 1)$ should be included if $g_{\alpha j}^{\mathrm{rel}} - g_{\alpha j}^{\mathrm{eq}}$ is used instead.

Here, we verify the divergence-free condition for $\vec{B}$ using three methods. Firstly, the divergence can be computed from a local summation: $\nabla \cdot \vec{B} = \frac{-1}{\Delta t \tau_g c_g^2} \left(\Lambda_{jj} - \Lambda_{jj}^{\mathrm{eq}} \right) = \frac{-1}{\Delta t \tau_g c_g^2} \Lambda_{jj}$ [18]. Secondly, the gradient of an arbitrary scalar φ can be computed by the LBM inherent discretisation scheme using a summation over the nearest grid points: $\partial \varphi / \partial x_i = \frac{3}{c \Delta x} \sum_{\alpha=0}^{Q-1} \omega_\alpha e_{\alpha i} \varphi(\vec{x} + \vec{e}_\alpha \Delta t)$, which can also be used to compute the divergence of an arbitrary vector by considering each vector component separately [10]. Thirdly, $\nabla \cdot \vec{B}$ can also be computed from a finite difference scheme. Case 2 studied in Section 5.2 (see Fig. 5) is used for verification. The steady-state divergence using the consistent model [25] is shown in Fig. A1, demonstrating $\nabla \cdot \vec{B} \approx 0$ with each of the three divergence computation schemes. Note that the largest values of $\left| \nabla \cdot \vec{B} \right| \approx 10^{-6}$ occur around the conducting walls, while the divergence is much smaller in the domain interior. Therefore, the kinetic solver for $\vec{B}$ will have better accuracy in enforcing $\nabla \cdot \vec{B} = 0$ for problems where all boundaries are periodic, and the influence of various boundary conditions can be completely removed.

The magnetic boundary condition has been comprehensively studied in Ref. [28]. The insulating walls with $\vec{B} = \vec{B}_{\mathrm{ext}}$ are modelled by the halfway anti-bounce-back scheme for $\vec{g}_\alpha$, while the perfectly conducting walls with $\partial \vec{B} / \partial n = 0$ are modelled by the halfway bounce-back scheme. A modification for moving walls is provided and the on-node moment-based scheme is also derived in the reference. Additionally, extensions have been made to implement the Shercliff thin-wall boundary condition for high-fidelity simulations of the wall effects of finite electrical conductivity, which will be considered in future work.

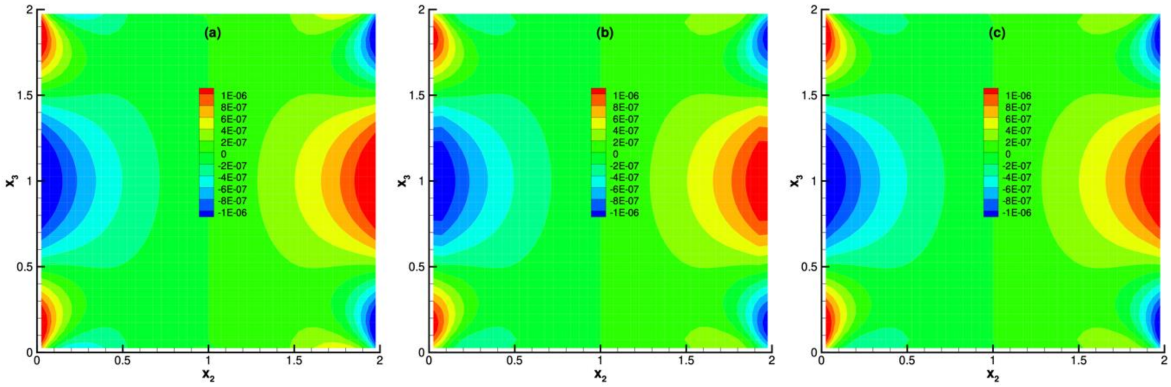

Fig. A1. Verification of $\nabla \cdot \vec{B} = 0$ in Case 2 with the magnetic field divergence computed by (a) the local summation scheme, (b) the nearest-grid-points summation scheme, and (c) the finite difference scheme.

REFERENCES

[1] S. Chen and G. D. Doolen, “Lattice Boltzmann method for fluid flows,” *Annu. Rev. Fluid Mech.,* vol. 30, p. 329–364, 1998.

[2] C. K. Aidun and J. R. Clausen, “Lattice-Boltzmann method for complex flows,” *Annu. Rev. Fluid Mech.,* vol. 42, p. 439–472, 2010.

[3] Z. Guo and C. Shu, Lattice Boltzmann method and its application in engineering, World Scientific, 2013.

[4] J. Zhang, “Lattice Boltzmann method for microfluidics: models and applications,” *Microfluid. Nanofluid.,* vol. 10, p. 1–28, 2011.

[5] C. Pan, M. Hilpert and C. T. Miller, “Lattice-Boltzmann simulation of two-phase flow in porous media,” *Water Resour. Res.,* vol. 40, p. W01501, 2004.

[6] Q. Kang, P. C. Lichtner and D. Zhang, “Lattice Boltzmann pore-scale model for multicomponent reactive transport in porous media,” *J. Geophys. Res.-Sol. Ea.,* vol. 111, p. B05203, 2006.

[7] H. Liu, Q. Kang, C. R. Leonardi, S. Schmieschek, A. Narváez, B. D. Jones, J. R. Williams, A. J. Valocchi and J. Harting, “Multiphase lattice Boltzmann simulations for porous media applications: A review,” *Computat. Geosci.,* vol. 20, p. 777–805, 2016.

[8] Y.-L. He, Q. Liu, Q. Li and W.-Q. Tao, “Lattice Boltzmann methods for single-phase and solid-liquid phase-change heat transfer in porous media: A review,” *Int. J. Heat Mass Tran.,* vol. 129, p. 160–197, 2019.

[9] Q. Li, K. H. Luo, Q. J. Kang, Y. L. He, Q. Chen and Q. Liu, “Lattice Boltzmann methods for multiphase flow and phase-change heat transfer,” *Prog. Energ. Combust.,* vol. 52, p. 62–105, 2016.

[10] J. Li, D.-V. Le, H. Li, X. Zhang, C.-W. Kang and J. Lou, “Hybrid outflow boundary condition for the pseudopotential LBM simulation of flow boiling,” *Int. J. Therm. Sci.,* vol. 196, p. 108741, 2024.

[11] D. O. Martínez, S. Chen and W. H. Matthaeus, “Lattice Boltzmann magnetohydrodynamics,” *Phys. Plasmas,* vol. 1, p. 1850–1867, 1994.

[12] M. J. Pattison, K. N. Premnath, N. B. Morley and M. A. Abdou, "Progress in lattice Boltzmann methods for magnetohydrodynamic flows relevant to fusion applications," *Fusion Eng. Des.,* vol. 83, p. 557–572, 2008.

[13] P. R. Hays and J. S. Walker, "Liquid-metal MHD open-channel flows," *J. Appl. Mech.,* vol. 51, p. 13–18, 1984.

[14] N. B. Morley and M. A. Abdou, "Study of fully developed, liquid-metal, open-channel flow in a nearly coplanar magnetic field," *Fusion Technol.,* vol. 31, p. 135–153, 1997.

[15] D. Gao, N. Morley and V. Dhir, "Numerical study of liquid metal film flows in a varying spanwise magnetic field," *Fusion Eng. Des.,* vol. 63–64, p. 369–374, 2002.

[16] N. B. Morley, S. Smolentsev, L. Barleon, I. R. Kirillov and M. Takahashi, "Liquid magnetohydrodynamics — recent progress and future directions for fusion," *Fusion Eng. Des.,* vol. 51–52, p. 701–713, 2000.

[17] N. B. Morley, S. Smolentsev, R. Munipalli, M.-J. Ni, D. Gao and M. Abdou, "Progress on the modeling of liquid metal, free surface, MHD flows for fusion liquid walls," *Fusion Eng. Des.,* vol. 72, p. 3–34, 2004.

[18] P. J. Dellar, "Lattice kinetic schemes for magnetohydrodynamics," *J. Comput. Phys.,* vol. 179, no. 1, p. 95–126, 2002.

[19] A. De Rosis, "Nonorthogonal central-moments-based lattice Boltzmann scheme in three dimensions," *Phys. Rev. E,* vol. 95, p. 013310, 2017.

[20] H. Yamaguchi, X.-D. Niu and X.-R. Zhang, "Investigation on a low-melting-point gallium alloy MHD power generator," *Int. J. Energy Res.,* vol. 35, p. 209–220, 2011.

[21] G. Breyiannis and D. Valougeorgis, "Lattice kinetic simulations of 3-D MHD turbulence," *Comput. Fluids,* vol. 35, p. 920–924, 2006.

[22] A. De Rosis, R. Liu and A. Revell, "One-stage simplified lattice Boltzmann method for two- and three-dimensional magnetohydrodynamic flows," *Phys. Fluids,* vol. 33, p. 085114, 2021.

[23] B. Magacho, H. S. Tavares, L. Moriconi and J. B. R. Loureiro, "Double multiple-relaxation-time model of lattice-Boltzmann magnetohydrodynamics at low magnetic Reynolds numbers," *Phys. Fluids,* vol. 35, p. 013610, 2023.

[24] R. Foldes, E. Lévêque, R. Marino, E. Pietropaolo, A. DeRosis, D. Telloni and F. Feraco, "Efficient kinetic Lattice Boltzmann simulation of three-dimensional Hall-MHD Turbulence," *J. Plasma Phys.,* vol. 89, no. 4, p. 905890413, 2023.

[25] G. Vahala, B. Keating, M. Soe, J. Yepez, L. Vahala, J. Carter and S. Ziegeler, "MHD turbulence studies using lattice Boltzmann algorithms," *Commun. Comput. Phys.,* vol. 4, no. 3, p. 624–646, 2008.

[26] P. J. Dellar, "Moment equations for magnetohydrodynamics," *J. Stat. Mech.,* p. P06003, 2009.

[27] P. J. Dellar, "Bulk and shear viscosities in lattice Boltzmann equations," *Phys. Rev. E,* vol. 64, p. 031203, 2001.

[28] E. Yahia and K. Premnath, "On boundary conditions for lattice kinetic schemes for magnetohydrodynamics bounded by walls with finite electrical conductivities," *arXiv,* p. 2112.13930, 2021.

[29] Z. Guo, C. Zheng and B. Shi, "An extrapolation method for boundary conditions in lattice Boltzmann method," *Physics of Fluids,* vol. 14, p. 2007–2010, 2002.

[30] A. Kupershtokh, D. Medvedev and D. Karpov, "On equations of state in a lattice Boltzmann method," *Comput. Math. Appl.,* vol. 58, p. 965–974, 2009.

[31] M.-J. Ni, R. Munipalli, P. Huang, N. B. Morley and M. A. Abdou, "A current density conservative scheme for incompressible MHD flows at a low magnetic Reynolds number. Part II: On an arbitrary collocated mesh," *J. Comput. Phys.,* vol. 227, p. 205–228, 2007.

[32] A. De Rosis, R. Huang and C. Coreixas, "Universal formulation of central-moments-based lattice Boltzmann method with external forcing for the simulation of multiphysics phenomena," *Physics of Fluids,* vol. 31, p. 117102, 2019.